Research article

Enhanced ferro-photocatalytic performance for ANbO₃ (A = Na, K) nanoparticles

Yu Huan [1,*], Hengtao Shen [1], Yuanna Zhu[1], Min Li[1], Hangyu Li[1], Zhenxing Wang[1], Yanan Hao [2,*] and Tao Wei[1]

[1] School of Material Science and Engineering, University of Jinan, Jinan 250022, China
[2] State Key Laboratory of Information Photonics and Optical Communications & School of Science Beijing University of Posts and Telecommunications Beijing 100876, P. R. China

* **Correspondence:** Email: mse_huany@ujn.edu.cn; hyn@bupt.edu.cn

Abstract: In this study, NaNbO₃ with average grain size of ~50 nm and KNbO₃ with average grain size of ~300 nm nanocrystals are prepared by the water-based citrate precursor sol-gel process. However, the KNbO₃ sample exhibits better photocatalytic performance than that of the NaNbO₃ sample by Rh B degradation experiment. By Rietveld refinements and piezoelectric displacement measurements, the KNbO₃ with the space group of Bmm2 is ferroelectric while the NaNbO₃ with the space group of Pbma is antiferroelectric. The polarization-modulated built-in electric fields in the ferroelectric KNbO₃ nanoparticles can efficiently enhance the separation of photo-generated charge carries and thus improve the photocatalytic activity. However, there is no internal electric field in the antiferroelectric grain because of the antiparallel spontaneous polarization in the adjacent unit cell. Therefore, KNbO₃ exhibits better oxidizing ability of organic dyes than NaNbO₃. The ferroelectric KNbO₃ nanoparticles exhibit an optimum photocatalytic performance for a complete degradation of Rh B in 100 min under UV-Vis light irradiation with auxiliary ultrasonic excitation. This study demonstrates that the perovskite-type ferroelectric nanocrystals are potentially to design high-performance catalysts for degradation of contaminant.

Keywords: ferroelectric; antiferroelectric; nanoparticle; photocatalysis; internal electric field

1. Introduction

Semiconductor photocatalysts can directly convert solar energy to chemical energy, which have

attributed remarkable attention due to the environmental remediation and increasing energy demands. Recently, the perovskite-type materials with the chemical formula of ABO_3, such as $BaTiO_3$ [1], $SrTiO_3$ [2], $KNbO_3$ [3,4], $NaTaO_3$ [5], $BiFeO_3$ [6], and $PbTiO_3$ [7], are investigated as photocatalysts to degrade the organic contaminant because of their good stability and low toxicity [8,9]. Among them, the ferroelectric perovskite-type materials can enhance the photocatalytic performance on account of the polarization-modulated built-in electric field, which can effectively separate excited electron/hole pairs. In addition, the ferroelectric materials can be used to fabricate many electron devices, such as energy harvester [10], energy storage [11], force sensor [12], electronic actuator etc. [13–16]. It may provide insights into strategies for designing multi-functional piezo-/ferroelectric devices combined with catalytic degradation of pollutants.

However, the photocatalytic activity of these perovskite-type ferroelectric materials is still very low compared with some famous semiconductor photocatalysts, such as TiO2 [17–19]. To improve the photocatalytic activity is the primary task to accelerate the development of ferro-photocatalysts. One of the most common methods is loading well-dispersed noble metal nanocrystals, such as Pt, Au, Ag etc., on the ferroelectric particles to utilize their localized surface plasmon resonance [20]. But these noble metals are costly. Another common approach is to decrease the particle size and increase the surface areas [21]. On one hand, the number of defects on the surface increases with the decreasing particle size. The defects operate as trapping and recombination centers between photon-generated electrons and holes, which can decrease the recombination probability [22]. On the other hand, when the particle size is reduced to nanoscale, the migration distance of the photon-generated carriers from interior to the surface becomes shorter [21,23]. Therefore, we aim to prepare the nanoscale ferroelectric crystals to improve the photocatalytic activity.

Compared with the Pb-based ferroelectric materials, the $ANbO_3$ (A = K, Na) materials are environmentally friendly and are harmless to human [10,24]. In this study, $NaNbO_3$ with average grain size of ~50 nm and $KNbO_3$ with average grain size of ~300 nm nanocrystals are prepared by the water-based citrate precursor sol-gel process. Their photocatalytic performances are systematically studied by the degradation of Rhodamine B (Rh B). By XRD structural refinement, the ferroelectric $KNbO_3$ (Bmm2) and antiferroelectric $NaNbO_3$ (Pbma) nanoparticles with good crystallinity are synthesized. Amazingly, compared with the antiferroelectric $NaNbO_3$, the ferroelectric $KNbO_3$ nanoparticles with larger particle size exhibit better photocatalytic activity. It demonstrates the polarization-modulated built-in electric fields in the ferroelectric particles can efficiently enhance the photocatalytic activity.

2. Materials and method

All the solvents and raw materials were analytically pure and used without any further purification. $KNbO_3$ nanoparticles (KN) and $NaNbO_3$ nanoparticles (NN) were prepared by the water-based sol-gel method. Firstly, the 0.05 mol niobium hydroxide ($Nb(OH)_5$, 99.95%) was dissolved in 200 ml aqueous solution of 0.15 mol oxalic acid ($(COOH)_2 \cdot 2H_2O$, 99.5%) which was stirred vigorously at 50 ℃ for 5 h to form transparent solution. Then 0.05 mol alkali carbonate (K_2CO_3 or Na_2CO_3, 99.8%) was added. After stirring for 2 h at 50 ℃, 0.1 mol citric acid ($C_6H_8O_7 \cdot H_2O$, 99.5%) was added to the solution and ammonia solution ($NH_3 \cdot H_2O$, 25.0–28.0%) was used to adjust the PH value to 5–7. After 2 h stirring, a stable colorless transparent sol was gained. Subsequently, the sol was heated at 100 ℃ to prepare the transparent yellow gel. Finally, the gel was

calcined in air to obtain the nanoparticles.

Thermogravimetric-differential scanning calorimetry analysis (TG-DSC) was carried out on STA 449 F3 (Netzsch, Germany) under a 20 mL/min air flow with heating rate of 10 °C/min. Transmission electron microscopy (TEM), high-resolution transmission electron microscopy (HRTEM) and selected area electron diffraction (SAED) were carried out on TECNAI G^2 20 (FEI, USA) at 200 kV. X-ray diffraction (XRD) was measured by Smartlab (Rigaku, Japan) using Cu Kα radiation. High-resolution X-ray photoelectron spectroscopy (XPS) data were obtained using an ESCALab 250 Xi electron spectrometer (Thermo Fisher Scientific, USA). Fourier transform infrared spectra (FTIR) were recorded on a VERTEX 70V spectrometer (Bruker, Germany) using KBr pellet method in the range of 400 to 4000 cm^{-1}. Micro-Raman spectra were measured on a Confocal LabRAM HR800 spectrometer system (JY, France) in the range of 100 to 1500 cm^{-1}. Atomic force microscopy (AFM) measurements and the corresponding displacement as a function of direct voltage in a range from 0 to 10 V of the individual particles were carried out with a scanning probe microscopy system (SPM, SPI4000&SPA300HV, Seiko, Tokyo, Japan) with a conductive Pt-coated Si cantilever (SI-DF3). The Brunauer-Emmett-Teller (BET) specific surface was measured using a QUADRASORB SI (Quantachrome, USA). Diffuse reflectance ultraviolet and visible (UV-Vis) spectra were obtained using a Perkin Elmer Lambda 950 UV/Vis/NIR spectrometer (Perkin Elmer, USA) with a 150 mm Int. Sphere. Fine BaSO$_4$ powder was used as a standard, and the spectra were recorded in the range of 100 to 1200 nm. The photocurrent measurement was conducted on an electrochemical system (CHI 660E, Shanghai, China) under the radiation of 300W Xe lamp using a standard three-electrode cell with a working electrode, a platinum wire counter electrode, and a standard calomel electrode reference electrode. 1 M Na$_2$SO$_4$ aqueous solution was used as the electrolyte solution. The working electrode was prepared according to the following process. Twenty milligrams of as-prepared sample was suspended in 0.5 mL ethanol, and then dip-coated on a 10 mm × 20 mm indium-tin oxide (ITO) glass electrode. The electrode was then annealed at 100 °C for 1 h in vacuum.

The photocatalytic activity of the as-prepared samples for the degradation of Rhodamine B (RhB, 99.9%) in aqueous solutions was evaluated. Prior to irradiation, 0.1 g powders was mixed with RhB (100mL, with a concentration of 0.02 mM/L) in a 100-mL Pyrex flask and then sonicated in a cool water bathe for 10 min. Afterwards, the suspensions was magnetically stirred to reach a complete adsorption-desorption equilibrium. The flask was subsequently exposed to UV-Vis light irradiation with maximum illumination time up to 240 min. During the irradiation, the suspension was magnetically stirred and the reaction temperature was kept at room temperature. The excitation source is a 300 W mercury lamp located at *ca.* 15 cm away from the flask. At certain time intervals, about 3.5 mL aliquots were sampled and centrifuged. The absorption intensity of RhB at 554 nm was measured to reflect the dye concentration on a PerkinElmer Lambda 950 UV-Vis spectrometer (Perkin Elmer, USA).

3. Results and discussion

TG-DSC curves of the KN and NN gel are carried out to explore the calcining temperature as displayed in figures 1a and 1b. A large weight loss from 200 °C to 400 °C accompanied by an exothermic peak is due to the citrate and oxalate complexes decomposition and combustion [25]. When the temperature further increases to ~700 °C, residual organic compounds combust. The
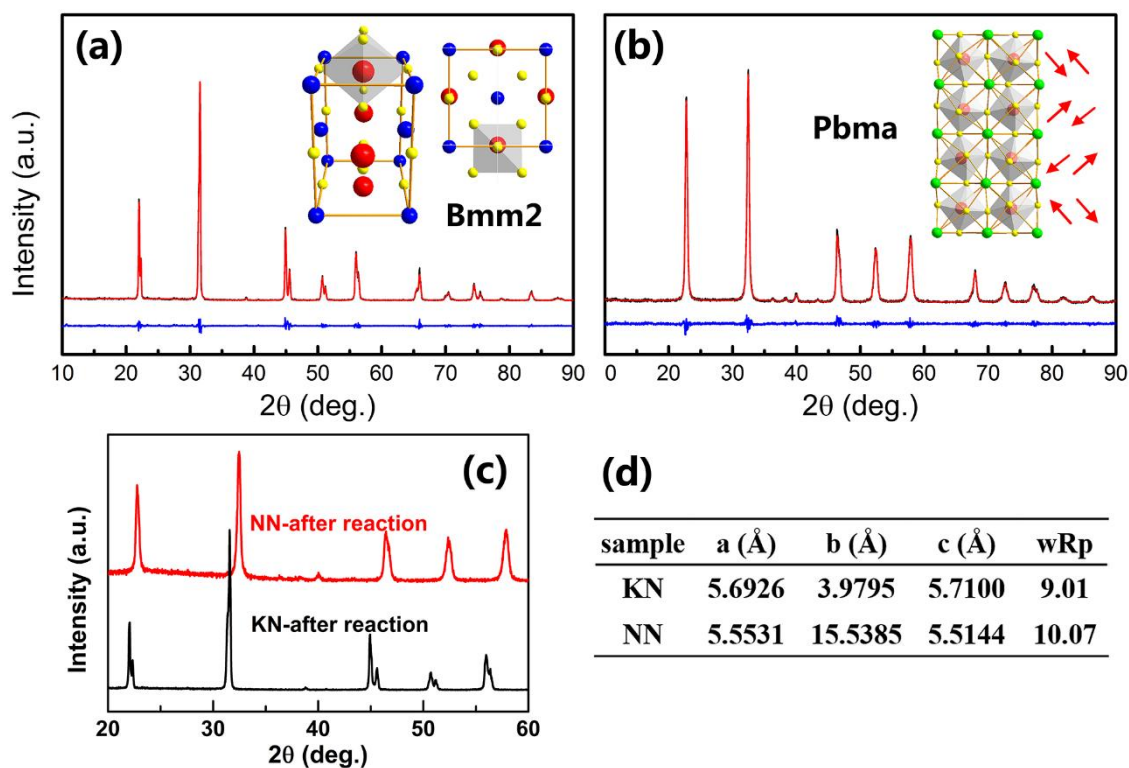
distinct endothermic peak at ~660 °C and ~525 °C should be ascribed to the crystallization of KN and NN, respectively. Therefore, the calcining temperatures of KN and NN gels are set as 750 °C and 650 °C, respectively, in this work.
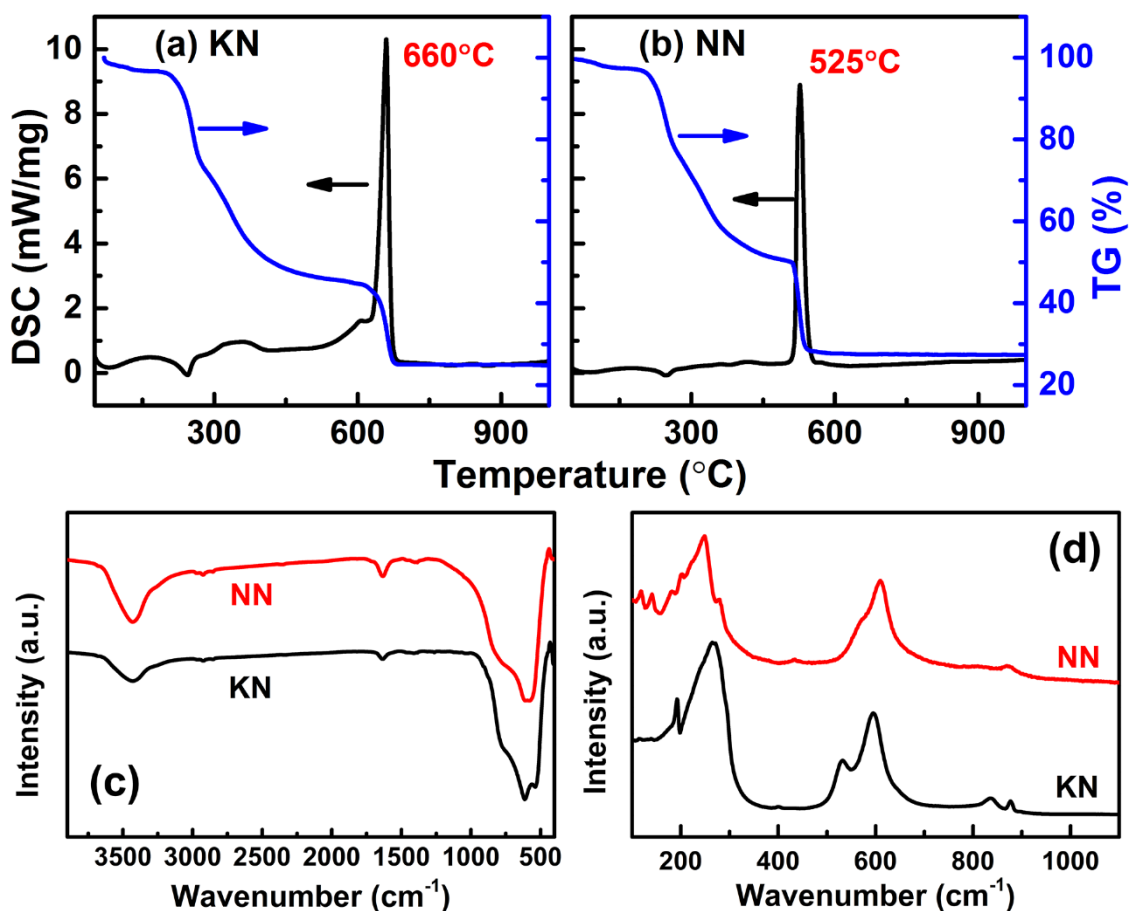
Figure 1. TG-DSC curves of (a) KN gel and (b) NN gel; (c) FTIR spectra and (d) micro-Raman spectra of KN and NN particles.

FTIR spectra of the calcined KN and NN powders are displayed in figure 1c. The weak absorption bands at 3438 and 1639 cm^{-1} are ascribed to H_2O or OH^- on the surface of samples. The band at 1393 cm^{-1} can be assigned to the CO_2 absorbed on the sample. The characteristic absorption bands in the region from 225 to 850 cm^{-1} attribute to the NbO_6 octahedron [26]. The band around 500 cm^{-1} can be assigned to the edge-shared NbO_6 octahedron and the strong band centered at 623 cm^{-1} represents O–Nb–O stretching vibrations in the corner-shared NbO_6 octahedron [27], demonstrating the formation of the perovskite structure. Figure 1d displays the micro-Raman spectra of KN and NN powders. Raman shifts in the range of 100–800 cm^{-1} well coincide well with the Raman phonon modes of the orthorhombic $KNbO_3$ and $NaNbO_3$ with respect to Ref. [3,13,28]. ν1 (~598 cm^{-1}) and ν2 (~540 cm^{-1}) represent the O–Nb–O stretching vibration, while ν5 (260 and 245 cm^{-1} for KN and NN, respectively) is ascribed to the vibration of the edge-shared NbO_6. The little different Raman shifts of ν5 for KN and NN powders should attribute to their different crystal structure, which would be investigated by XRD analysis. In addition, the sharp Raman shifts confirm the good crystallinity of the as-prepared KN and NN nanoparticles. No characteristic peaks of the

organic functional groups are found in the FTIR and Raman spectra, which means that the organics have been removed completely after the KN and NN gels being calcined at 750 ℃ and 650 ℃, respectively.

Figure 2. Experimental (black line), calculated (red line), and difference (blue line) plots of (a) KN and (b) NN samples as obtained by Rietveld refinement; Insets are illustrations of the corresponding $KNbO_3$ (space group: Bmm2) and $NaNbO_3$ (space group: Pbma) crystal structure; (c) XRD patterns of KN and NN powder after photocatalytic reaction; (d) Rietveld refined parameters of KN and NN powders.

Figures 2a and 2b are the XRD patterns of KN and NN powders, respectively, which exhibit a pure perovskite and good crystallinity [29]. The diffraction peaks of the NN powders are obviously broader than that of the KN powders, demonstrating that the grain size of the NN particles is smaller. To elucidate further the phase structure of the as-synthesized nanopowders, the XRD data of KN and NN powders are analyzed by Rietveld refinements using GSAS software on the basis of Bmm2 and Pbma space groups, respectively. The refined lattice parameters are given in figure 2d. The calculated and experimental lines exhibit an excellent agreement, indicating that the space groups are reliable. The corresponding crystal structures are illustrated in insets of figures 2a and 2b. From the front view of the KN, it can be found that the Nb^{5+} is not precisely located at the center of oxygen octahedrons, which confirms the ferroelectric properties of the as-prepared KN particles. From the front view of the NN, it can be found that the spontaneous polarization also exists in the unit cell, and the direction is depicted by the red arrows in figure 2b. However, the spontaneous polarization direction of the neighboring unit cell is antiparallel. The adjacent dipoles cancel each other out and the macroscopic spontaneous polarization is zero. Therefore, the as-synthesized NN material in this

work is antiferroelectric.
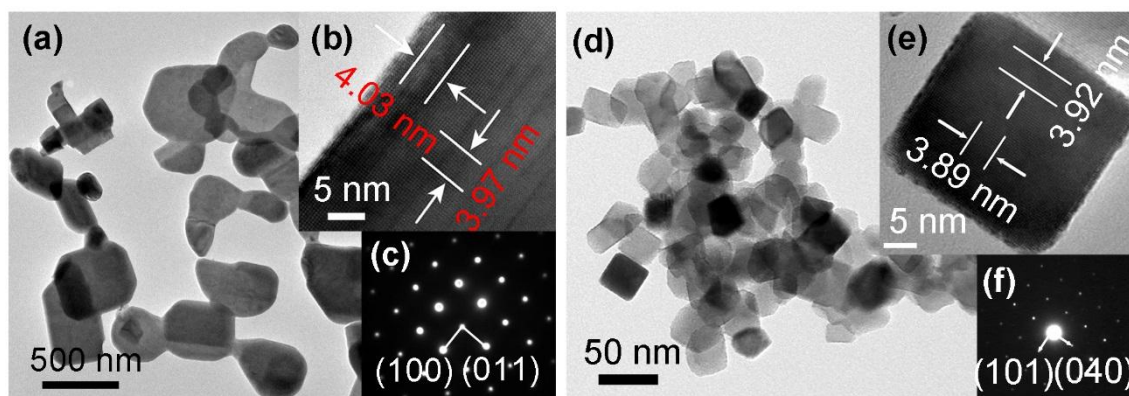
Figure 3. (a) TEM and (b) HRTEM images of KN nanoparticles, (c) SAED patterns obtained from the region in figure b. (c) TEM and (d) HRTEM images of NN nanoparticles, (e) SAED patterns obtained from the region in figure e.

The morphological feature and crystal structure of the as-synthesized particles are characterized using TEM, HRTEM and SAED as shown in figure 3. The KN sample has irregular morphology with average size 200 ~ 500 nm in figure 3a. A clear lattice fringe and diffraction spot can be detected from the HRTEM and SAED images, respectively, demonstrating the good crystallinity of the KN particles. In addition, the crystal lattice spacings marked in figure 3b are 0.403 and 0.397 nm, which correspond to (011) and (100) crystal planes of orthorhombic $KNbO_3$ (JCPDS No. 71-2171), respectively. The angle of the adjacent spots labeled in the SAED pattern is 90°, which is identical to the theoretical included angle of the (011) and (100) planes. By comparison, NN particles are cube-like morphology with smaller average size of ~30 nm in figure 3d. The interplanar lattice spacings of 0.392 nm and 0.389 nm in figure 3e match well with the (101) and (004) atomic planes, respectively, of the orthorhombic $NaNbO_3$ (JCPDS No. 89-8957) [30]. As depicted in figure 3f, the corresponding SAED pattern exhibits good crystalline. The included angle of the adjacent spots labeled in the SAED pattern is 90°, which is identical to the theoretical included angle between the (101) and (004) planes.

XPS spectra are carried out to investigate the surface composition and valence state of the as-prepared samples in figure 4. The peaks located at ~291.2 eV, ~1070.9 eV, and ~206.6 eV are attributed to K 2p, Na 1s, and Nb 3d core level peaks, respectively as shown in the survey scanning XPS spectra in figures 4a and 4d. No additional peaks can be detected. In addition, the peak positions of K $2p_{3/2}$, Na 1s, and Nb $3d_{5/2}$ correspond to K^+, Na^+, and Nb^{5+} oxidation state, respectively, in good agreement with those of pure $KNbO_3$ and $NaNbO_3$ obtained in previous works [3,31]. The XPS spectra verify the formation of $KNbO_3$ and $NaNbO_3$.

Table 1. BET surface areas and band energy gap of KN and NN nanoparticles.

Samples	BET (m^2/g)	Band gap (eV)
KN	7.368	3.74
NN	17.466	3.79
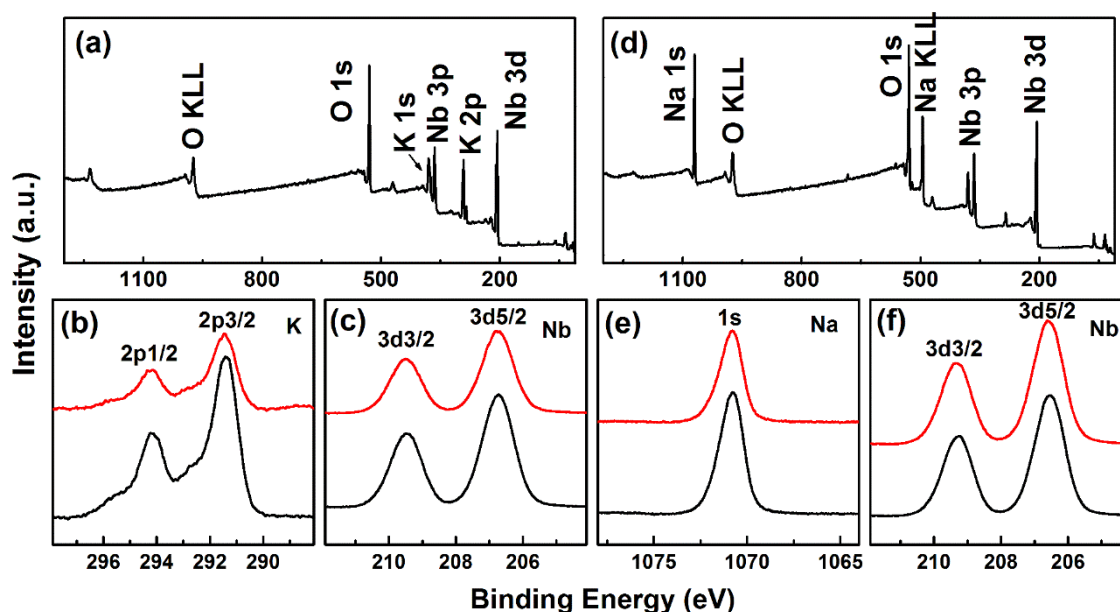
Figure 4. XPS spectra of the KN sample: (a) survey scan, (b) K 2p, (c) Nb 3d core-level; XPS spectra of the NN sample: (a) survey scan, (b) Na 1s, (c) Nb 3d core-level. (Notes: top and bottom lines are the XPS spectra of the KN and NN samples before and after photocatalytic reaction, respectively.)
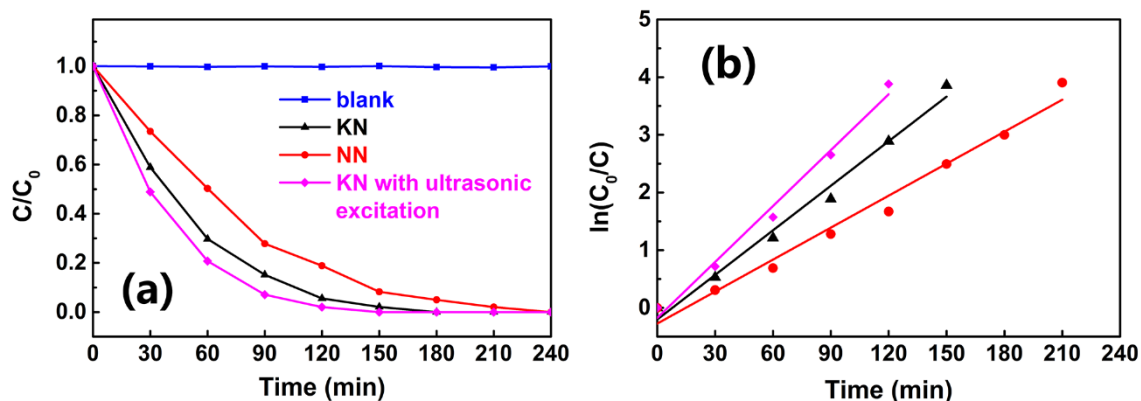

Figure 5. (a) Photodegradation curves of RhB aqueous solutions catalyzed by the photocatalyst; (b) linear least-squares fitting of $\ln(C/C_0)$ versus irradiation time plots.

The photocatalytic activity of as-prepared samples is evaluated by RhB degradation under UV-Vis light illumination. The change of relative RhB concentration as a function of irradiation time is shown in figure 5a. RhB degradation under UV-Vis light illumination is negligible as observed by the blank experiment. When the photocatalysts are added in the aqueous solution, the RhB aqueous solution concentration decreases rapidly, suggesting that RhB has been destroyed. To evaluate the photocatalytic activity quantitatively, the reaction rate constants are calculated. The photodegradation of RhB with KN and NN materials can be considered as a pseudo-first-order reaction [26], and their kinetics can be expressed as follows:

$$C = C_0 e^{-kt} \qquad\qquad (1)$$

where k is the degradation rate constant, and C_0 and C are the initial concentrations of RhB and that at the irradiation time t, respectively. Figure 5b shows the linear relationship between $\ln(C_0/C)$ and t. The degradation rate constants for RhB aqueous solutions with the KN and NN are 0.02576 min^{-1}, 0.01848 min^{-1}, respectively. BET surface areas determined from nitrogen adsorption–desorption isotherms are listed in Table 1. The reaction rate constant per unit area of KN (0.0035 g m^{-2} min^{-1}) is much higher than that of NN nanoparticles (0.00106 g m^{-2} min^{-1}). Both of them demonstrate that the photocatalytic activity of KN is much higher than that NN nanoparticles in our study.

Generally speaking, photocatalytic activity should enhance with the decreasing particle size [21]. On one hand, the defect concentration on the surface increases with the decreasing particle size, where the defects can trap the photon-generated carriers and decrease their recombination probability [22]. On the other hand, the migration distance of the photon-generated carriers from interior to the surface becomes shorter for the nanoparticles [21,23]. From the above-mentioned TEM images, broaden X-ray diffraction peak, and BET (~7.368 m^2/g and ~17.466 m^2/g for KN and NN powders, respectively), it can be found that the particle size of NN is much smaller than that of KN. However, the KN sample exhibits better photocatalytic performance than that of the NN sample.
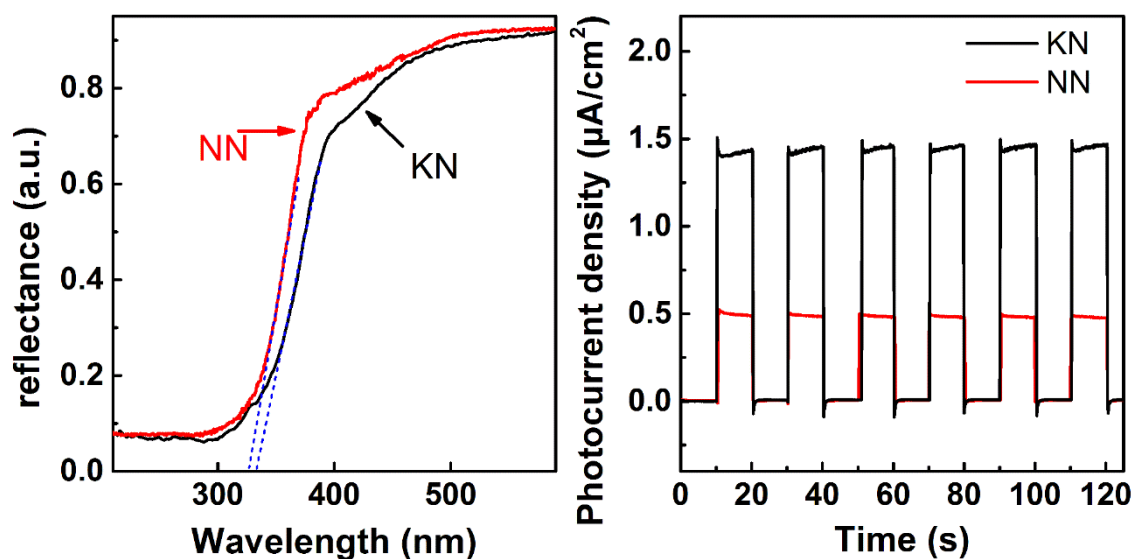
Figure 6. (a) UV–vis diffusion reflectance spectra (b) photocurrent density under UV–vis irradiation of KN and NN powders.
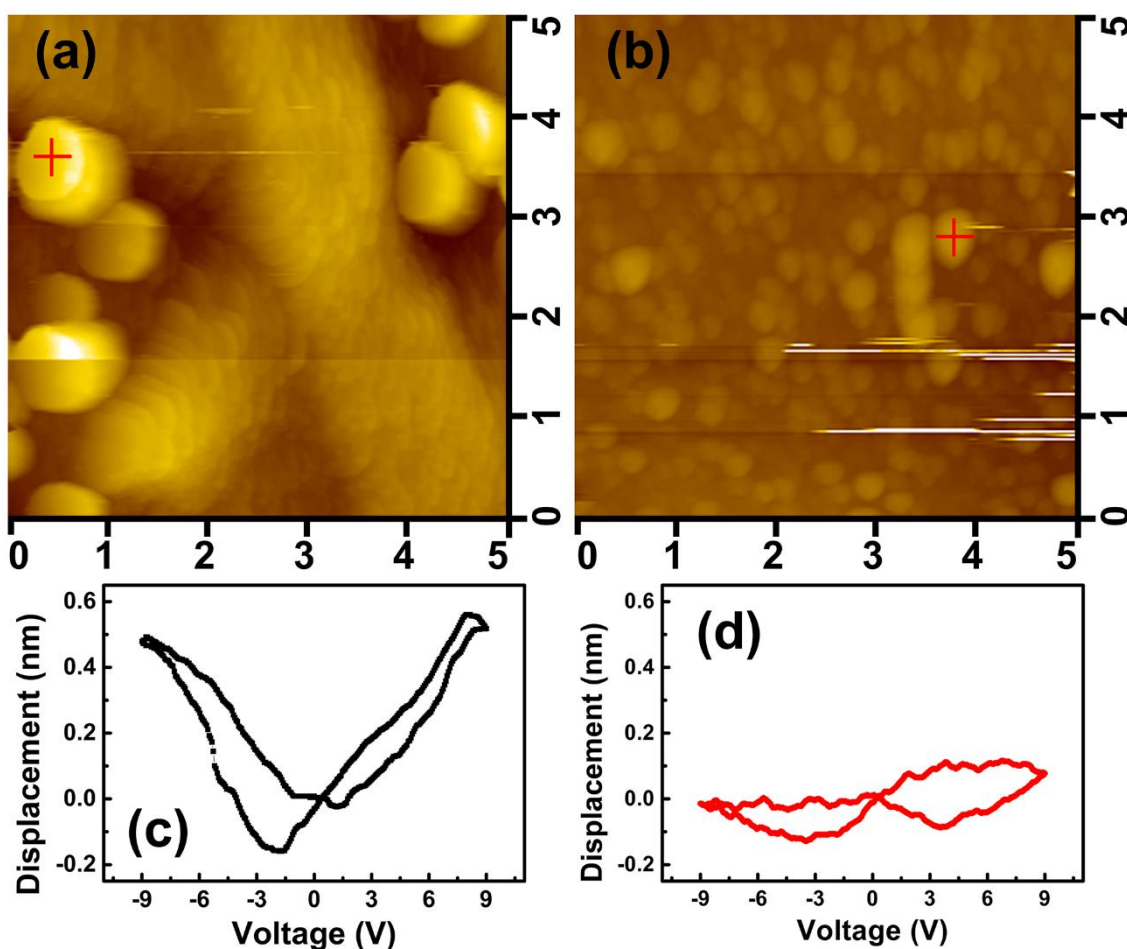
Figure 7. AFM images of (a) KN and (b) NN nanoparticles nanofiber; piezoelectric displacement curves as a function of direct voltage of (c) KN and (d) NN nanoparticles.

To elucidate the different photoactivity of the KN and NN nanoparticles, the UV-Vis diffuse reflectance spectra and photocurrent density are compared in figure 6. The band structure of semiconductors is evaluated by UV-Vis diffuse reflectance spectra as following. The linear part of the spectral line is extended as the blue dotted line, and then the intersection on x-axis is obtained. Band energy (E_g) is estimated by dividing 1240 by the wavelength of the intersection [32], which is summarized in the Table 1. E_g (~3.74 eV) of the KN particles is little smaller than that of the NN particles (~3.79 eV). The small E_g of KN nanoparticles can utilize the illumination more efficiently, and then promote the photocatalytic activity [33]. The photocurrent is measured to explore the effective separation of the photo-generated charge carries. The photocurrent densities of the KN and NN samples are about 1.48 and 0.5 $\mu A/cm^2$, respectively. Therefore, the separation efficiency of the photo-generated electrons and holes in the interface for the KN sample is much higher than that for NN samples [34,35]. Considering that the higher particle size and smaller BET for the KN samples in this study, the ferroelectricity modulated built-in electric fields should be responsible for the enhanced photocatalysis.

From the crystal structure analysis, KN with the space group of Bmm2 has the spontaneous polarization in [110] crystal direction. It can generate the internal electric field due to the Nb ion displacement. However, NN with Pbma space group is antiferroelectric state. The antiparallel

spontaneous polarization in the adjacent unit cell cancel the internal electric field out. In order to ascertain the ferroelectricity of the as-prepared KN particles, piezoelectric displacement versus direct voltage curve is measured in figure 7. Firstly, KN or NN particles are ultrasonically dispersed in ethanol, and the suspension is dropped on the Pt-coated silicon (Pt/Ti/SiO$_2$/Si) substrates [36]. Subsequently, the substrates are dried to remove ethanol. As is seen from the AFM images in figures 7a and 7b, the KN and NN particles are well dispersed on the substrates. Meanwhile, the KN particle size is larger than the NN particles, in accordance with the TEM images. The conductive cantilever tip is fixed on region labelled by cross symbols in figures 7a and 7b to character the local ferroelectric properties. An alternating voltage from -9 V to 9V is applied on the interesting point. In the Meantime, the piezoelectric displacement is recorded simultaneously by laser as illustrated in figures 7c and 7d. The displacement–voltage loop of KN particles displays a typical butterfly shape, verifying that as-prepared KN sample is ferroelectric. The converse piezoelectric coefficient d_{33}^{*}, calculated by taking the derivative on the displacement–voltage curves, reaches ~90 pm/V. Whereas the piezoelectric displacement and the corresponding d_{33}^{*} of the NN particles are very low, indicating the anti-ferroelectricity of the as-prepared NN sample in this work. The polarization electric field can accelerate the separation and mobility of the photogenerated electrons and holes, which has been verified in ferroelectric BaTiO$_3$ [37]. Therefore, the photocatalytic reaction rate of the antiferroelectric NN is lower than that of ferroelectric KN.

The photocatalytic degradation of the KN sample is also investigated with auxiliary ultrasonic excitation in figure 5. The degradation rate constant is about 0.0442 min^{-1}, which is enhanced to be over 25%. It should be ascribed to the larger effective electric field under ultrasonic vibrations [1], which can enhance the separation of photogenerated electron-hole pairs and promote free radicals generations. To confirm the stability of the photocatalyst, the XRD patterns and XPS spectra of the KN and NN nanoparticles after the photocatalysis are measured in figures 2c and 4. It can be found that the crystal structure and binding energy of K, Na and Nb elements are almost the same with the previous results, indicating that KN and NN nanoparticles are very stable against chemical reaction during photocatalysis.

4. Conclusion

KN and NN nanoparticles are prepared by the water-based citrate precursor sol-gel process and their photocatalytic activity is evaluated by Rh B degradation. From the TEM, broaden XRD peak and BET analysis, the particle size of NN is much smaller than that of as-prepared KN in this work. However, the KN sample exhibits much better photocatalytic performance than that of the NN sample. By Rietveld refinements and piezoelectric displacement measurements, the KN with the space group of Bmm2 is ferroelectric while the NN with the space group of Pbma is antiferroelectric. The polarization-modulated built-in electric fields in the ferroelectric KN nanoparticles can efficiently enhance the separation of photo-generated charge carries and thus improve the photocatalytic activity. In addition, the KN exhibit high chemical stability during photocatalysis. The ferroelectric KN nanoparticles exhibits an optimum photocatalytic performance for a complete degradation of Rh B in 100 min under UV-Vis light irradiation with auxiliary ultrasonic excitation. This study demonstrates that the perovskite-type ferroelectric materials are potentially applied in photocatalysis and relevant areas.

Acknowledgments

Conflict of interest

The authors declared that they have no conflicts of interest to this work.

References

1. S. Xu, L. Guo, Q. Sun, et al., Piezotronic effect enhanced Plasmonic photocatalysis by AuNPs/BaTiO$_3$ heterostructures, *Adv. Funct. Mater.*, **1** (2019), 1808737.
2. G. N. Wang, P. Wang, H. K. Luo, et al., Novel Au/La-SrTiO$_3$ microspheres: superimposed effect of gold nanoparticles and lanthanum soping in photocatalysis, *Chem. Asian J.*, **9** (2014), 1854–1859.
3. D. Yu, Z. Liu, J. Zhang, et al., Enhanced catalytic performance by multi-field coupling in KNbO$_3$ nanostructures: Piezo-photocatalytic and ferro-photoelectrochemical effects, *Nano Energy*, **58** (2019), 695–705.
4. X. Zhang, Y. Huan, K. Li, et al., Enhanced photocatalytic activity and cycle stability driven by ultrasonic vibration for ferroelectric photocatalysts, *IET Nanodielectr.*, **2** (2019), 48–53.
5. C. C. Hu, C. C. Tsai and H. S. Teng, Structure characterization and tuning of perovskite-like NaTaO$_3$ for applications in photoluminescence and Photocatalysis, *J. Am. Ceram. Soc.*, **92** (2009), 460–466.
6. F. Gao, Y. Yuan, K. Wang, et al., Preparation and photoabsorption characterization of BiFeO$_3$ nanowires, *Appl. Phys. Lett.*, **89** (2006), 102506.
7. D. Arney, T. Watkins and P. A. Maggard, Effects of particle surface areas and microstructures on photocatalytic H$_2$ and O$_2$ production over PbTiO$_3$, *J. Am. Ceram. Soc.*, **94** (2011), 1483–1489.
8. E. Grabowska, Selected perovskite oxides: Characterization, preparation and photocatalytic properties: A review, *Appl. Catal. B-Environ.*, **186** (2016), 97–126.
9. B. Cui, P. Werner, T. Ma, et al., Direct imaging of structural changes induced by ionic liquid gating leading to engineered three-dimensional meso-structures, *Nat. Commun.*, **9** (2018), 3055.
10. Y. Huan, X. S. Zhang, J. N. Song, et al., High-performance piezoelectric composite nanogenerator based on Ag/(K,Na)NbO$_3$ heterostructure, *Nano Energy*, **50** (2018), 62–69.
11. Z. Feng, Y. Hao, M. Bi, et al., Highly dispersive Ba$_{0.6}$Sr$_{0.4}$TiO$_3$ nanoparticles modified P(VDF-HFP)/PMMA composite films with improved energy storage density and efficiency, *IET Nanodielectr.*, **1** (2018), 60–66.
12. K. Motoo, F. Arai, T. Fukuda, et al., Touch sensor for micromanipulation with pipette using lead-free (K,Na)(Nb,Ta)O$_3$ piezoelectric ceramics, *J. Appl. Phys.*, **98** (2005), 094505.
13. Y. Huan, T. Wei, Z. Wang, et al., Polarization switching and rotation in KNN-based lead-free piezoelectric ceramics near the polymorphic phase boundary, *J. Eur. Ceram. Soc.*, **39** (2019), 1002–1010.

14. T. Dippong, O. Cadar, E. A. Levei, et al., Effect of annealing on the structure and magnetic properties of $CoFe_2O_4$:SiO_2 nanocomposites, *Ceram. Int.*, **43** (2017), 9145–9152.

15. T. Dippong, E. A. Levei, O. Cadar, et al., Sol-gel synthesis of $CoFe_2O_4$:SiO_2 nanocomposites-insights into the thermal decomposition process of precursors, *J. Anal. Appl. Pyrolysis*, **125** (2017), 169–177.

16. T. Dippong, E. A. Levei, O. Cadar, et al., Thermal behavior of $Co_xFe_{3-x}O_4$/SiO_2 nanocomposites obtained by a modified sol–gel method, *J. Therm. Anal. Calorim.*, **128** (2017), 39–52.

17. C. C. Chen, W. H. Ma and J. C. Zhao, Semiconductor-mediated photodegradation of pollutants under visible-light irradiation, *Chem. Soc. Rev.*, **39** (2010), 4206–4219.

18. L. Guo, J. Deng, G. Wang, et al., Zn–air batteries: N, P-doped CoS_2 embedded in TiO_2 nanoporous films for Zn–Air batteries, *Adv. Funct. Mater.*, **28** (2018), 1870301.

19. T. Dippong, D. Toloman, E. A. Levei, et al., A possible formation mechanism and photocatalytic properties of $CoFe_2O_4$/PVA-SiO_2 nanocomposites, *Thermochim. Acta*, **666** (2018), 103–115.

20. P. Zhou, J. G. Yu and M. Jaroniec, All-solid-state Z-scheme photocatalytic systems, *Adv. Mater.*, **26** (2014), 4920–4935.

21. S. Rawalekar and T. Mokari, Rational design of hybrid nanostructures for advanced photocatalysis, *Adv. Funct. Mater.*, **3** (2013), 12–27.

22. T. Trindade, P. O'Brien and N. L. Pickett, Nanocrystalline semiconductors: Synthesis, properties, and perspectives, *Chem. Mater.*, **13** (2001), 3843–3858.

23. J. Y. Lan, X. Zhou, G. Liu, et al., Enhancing photocatalytic activity of one-dimensional $KNbO_3$ nanowires by Au nanoparticles under ultraviolet and visible-light, *Nanoscale*, **3** (2011), 5161–5167.

24. X. Zhang, Y. Huan, Y. Zhu, et al., Enhanced photocatalytic activity by the combined influence of ferroelectric domain and Au nanoparticles for $BaTiO_3$ fibers, *Nano*, **13** (2018), 1850149.

25. T. Dippong, E. A. Levei, O. Cadar, et al., Size and shape-controlled synthesis and characterization of $CoFe_2O_4$ nanoparticles embedded in a PVA-SiO_2 hybrid matrix, *J. Anal. Appl. Pyrolysis*, **128** (2017), 121–130.

26. Y. Huan, X. Wang, W. Hao, et al., Enhanced photocatalysis activity of ferroelectric $KNbO_3$ nanofibers compared with antiferroelectric $NaNbO_3$ nanofibers synthesized by electrospinning, *Rsc Adv.*, **5** (2015), 72410–72415.

27. T. T. Zhang, K. Zhao, J. G. Yu, et al., Photocatalytic water splitting for hydrogen generation on cubic, orthorhombic, and tetragonal $KNbO_3$ microcubes, *Nanoscale*, **5** (2013), 8375–8383.

28. Y. I. Yuzyuk, P. Simon, E. Gagarina, et al., Modulated phases in $NaNbO_3$: Raman scattering, synchrotron X-ray diffraction, and dielectric investigations, *J. Phys. Condens. Matter*, **17** (2005), 4977–4990.

29. C. Chaker, W. El Gharbi, N. Abdelmoula, et al., $Na_{1-x}Li_xNbO_3$ ceramics studied by X-ray diffraction, dielectric, pyroelectric, piezoelectric and Raman spectroscopy, *J. Phys. Chem. Solid*, **72** (2011), 1140–1146.

30. T. Y. Ke, H. A. Chen, H. S. Sheu, et al., Sodium niobate nanowire and its piezoelectricity, *J. Phys. Chem. C*, **112** (2008), 8827–8831.

31. H. You, X. Ma, Z. Wu, et al., Piezoelectrically/pyroelectrically-driven vibration/cold-hot energy harvesting for mechano-/pyro-bi-catalytic dye decomposition of $NaNbO_3$ nanofibers, *Nano Energy*, **52** (2018), 351–359.

32. J. Tauc, R. Grigorovici and A. Vancu, Optical properties and electronic structure of amorphous germanium, *Phys. Status Solidi*, **3** (1966), 37–46.

33. C. Dong, C. Lian, S. Hu, et al., Size-dependent activity and selectivity of carbon dioxide photocatalytic reduction over platinum nanoparticles, *Nat. Commun.*, **9** (2018), 1252.

34. J. Wang, L. Tang, G. Zeng, et al., 0D/2D interface engineering of carbon quantum dots modified Bi_2WO_6 ultrathin nanosheets with enhanced photoactivity for full spectrum light utilization and mechanism insight, *Appl. Catal. B Environ.*, **222** (2018), 115–123.

35. Y. Deng, L. Tang, G. Zeng, et al., Plasmonic resonance excited dual Z-scheme $BiVO_4/Ag/Cu_2O$ nanocomposite: synthesis and mechanism for enhanced photocatalytic performance in recalcitrant antibiotic degradation, *Environ. Sci. Nano*, **4** (2017), 1494–1511.

36. B. Cui, C. Song, H. J. Mao, et al., Magnetoelectric coupling induced by interfacial orbital reconstruction, *Adv. Mater.*, **27** (2015), 6651–6656.

37. J. Wu, N. Qin and D. Bao, Effective enhancement of piezocatalytic activity of $BaTiO_3$ nanowires under ultrasonic vibration, *Nano Energy*, **45** (2018), 44–51.